UC San Diego
UC San Diego Previously Published Works

Title
Impacts of the Hole Transport Layer Deposition Process on Buried Interfaces in Perovskite Solar Cells

Permalink
https://escholarship.org/uc/item/1d30r9ts

Journal
Cell Reports Physical Science, 1(7)

ISSN
2666-3864

Authors
Wang, Shen
Cabreros, Amanda
Yang, Yangyuchen
et al.
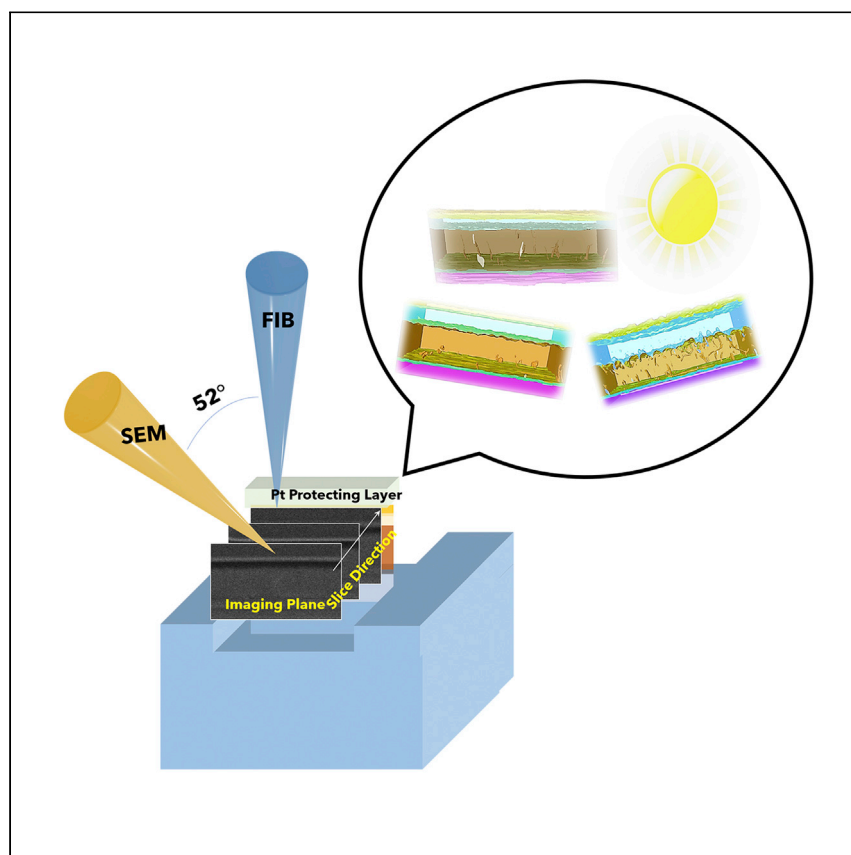
Publication Date
2020-07-01

DOI
10.1016/j.xcrp.2020.100103

Peer reviewed

Article

Impacts of the Hole Transport Layer Deposition Process on Buried Interfaces in Perovskite Solar Cells

Shen Wang, Amanda Cabreros, Yangyuchen Yang, ..., Øeystein Fjeldberg, David P. Fenning, Ying Shirley Meng

shirleymeng@ucsd.edu

HIGHLIGHTS

D morphology of perovskite solar cells (PSCs) is unveiled

FIB-SEM 3D reconstruction demonstrates the buried interfaces in PSCs

Hole transport layer dynamic spin coating can enhance PSCs' performance

Deposition of one film can influence all its connecting layers in PSCs

The perovskite solar cell (PSC) is a next-generation photovoltaic device. Here, Wang et al. identify the 3D structures of two PSCs deposited by different methods. This study suggests that the deposition methods not only influence the film's own properties but also those of its connected layers.

Article

Impacts of the Hole Transport Layer Deposition Process on Buried Interfaces in Perovskite Solar Cells

Shen Wang,[1] Amanda Cabreros,[1] Yangyuchen Yang,[2] Alexander S. Hall,[3] Sophia Valenzuela,[1] Yanqi Luo,[1] Juan-Pablo Correa-Baena,[4] Min-cheol Kim,[1] Øeystein Fjeldberg,[1] David P. Fenning,[1,2] and Ying Shirley Meng[1,2,5,*]

SUMMARY

Perovskite solar cells (PSCs) are one of the emerging solar cell technologies with high conversion efficiency. Several deposition methods had been applied for preparing their hole transport layer (HTL). However, there are few direct evidences to demonstrate whether HTL and its interfaces in PSCs have been influenced by the deposition methods. In this study, the 3D morphology of PSCs has been reconstructed by focused ion beam-scanning electron microscopy from the PSCs in which HTLs are deposited by different methods. The compositional distribution of HTLs is unveiled as well. All these associated layers and interfaces display obvious morphological and compositional differences that are attributed to the HTL components' solubility differences in the precursor solvent. Our investigation demonstrates the PSCs that HTL fabricated by dynamic spin-coating method have higher efficiency, better film uniformity, and less interfacial roughness than the static spin-coating-based devices.

INTRODUCTION

In 2009, the Miyasaka group applied halide-based perovskite materials as a sensitizer in liquid-dye-sensitized solar cells, thus beginning a new era for next-generation photovoltaic devices.[1] After an initial report by Grätzel, Park, and Snaith et al.,[2–7] various structures of the perovskite solar cells (PSCs) have been developed. Presently, the world record energy conversion efficiency for a single-junction PSC reached over 25.2%. This is the highest reported efficiency among all single-junction polycrystalline solar cells.[8–10] PSCs have prompted other perovskite device research: halide perovskite-based X-ray and gamma-ray detectors;[11–13] light-emitting diodes;[14–16] and smart windows.[17] Each broadens the perovskite energy conversion devices' territory.

As a p-i-n or n-i-p device, a PSC normally has three functional layers: perovskite absorption layer; electron transport layer (ETL); and hole transport layer (HTL). The qualities of these layers have strong impact on the device performance. Higher phase purity, greater density, and increased film uniformity can yield lower series resistance, higher shunt resistance, less current density-voltage (J-V) hysteresis, higher efficiency, and better long-term device stability.[18]

In PSC films, morphological measures—surface roughness, film thickness, and porosity—correlate with the PSC's performance. Generally, a dense, smooth, and

[1]Department of NanoEngineering, University of California, San Diego, 9500 Gilman Drive, La Jolla, CA 92093, USA

[2]Materials Science and Engineering Program, University of California, San Diego, 9500 Gilman Drive, La Jolla, CA 92093, USA

[3]Materials and Structural Analysis, Thermo Fisher Scientific, Houston, TX 77084, USA

[4]School of Materials Science and Engineering, Georgia Institute of Technology, Atlanta, GA 30332, USA

[5]Lead Contact

*Correspondence: shirleymeng@ucsd.edu

https://doi.org/10.1016/j.xcrp.2020.100103

uniform perovskite layer shows higher efficiency with less J-V curve hysteresis.[19,20] As most perovskite device layers are <1 µm thick, characterizing such layers requires high-resolution imaging.[21] Imaging techniques, such as scanning electron microscopy (SEM), scanning probe microscopy (SPM), focused ion beam (FIB), and (scanning) transmission electron microscopy ((S)TEM) have been widely applied for obtaining perovskite materials and devices morphological, compositional, and phase information.[22–26] SEM supplies surface and cross-section images of the perovskite devices and materials with nanoscale resolution and large depth of field in a vacuum. In combination with energy-dispersive X-ray spectroscopy (EDX), SEM also shows spatial elemental composition of perovskite materials and devices.[19] SPM, such as atomic force microscopy, reports the surface topography in air with angstrom-resolved z-position information. (S)TEM can yield resolutions greater than SEM in an ultra-high vacuum condition, but this technique requires a very thin sample (∼100 nm), and the electron beam can contaminate and degrade the sample. Recently, other mapping techniques have been applied to PSCs: synchrotron nanoprobe X-ray fluorescence (XRF);[27] Kelvin probe force microscopy (KPFM);[28] and electron-beam-induced current (EBIC).[29,30] Each method supplies further compositional, potential, and charge transfer and recombination information, thus allowing further correlation with device performance. Moreover, the combination of imaging hardware and software can supply even more information for various devices.[31]

Importantly, the above techniques normally supply 2D information for the device cross-section (SEM, FIB, and (S)TEM), 2D information of the top surface (SPM and SEM), or a 3D projected chemical composition in 2D using X-ray-based techniques (EDX and XRF). The 3D morphological information of the buried layers and interfaces, such as metal/HTL, perovskite/ETL, or perovskite/HTL interface, in PSCs at a high resolution remains hidden. Moreover, due to limited field of view at high resolution, one risk is inaccurately extrapolating intrinsic properties of samples from abnormal features. A more important fact is that these interfaces are crucial for the PSC's stability and efficiency. For example, in an n-i-p planer structure PSC, oxygen and water are diffused into the metal/HTL interface,[32,33] moisture-induced device degradation starts from the HTL/perovskite interface,[33] and photon-induced perovskite degradation happens at the ETL/perovskite interface.[34] The volumetric reconstruction of these buried interfaces and layers should illuminate detailed morphological information and its impacts on perovskite-based device performance.

Spin-coating is widely applied for depositing PSC functional layers in small area devices. As shown in Figure 1A, there are two different spin-coating methods, static spin-coating (or "static dispense") and dynamic spin-coating (or "dynamic dispense"). In a static spin-coating, the solution is loaded and fully wetted on the substrate before spinning process starts. After that, the solution and substrate are spun together to obtain the uniform film. In a dynamic spin-coating, the substrate is spinning at a desired speed. Solution is then quickly loaded (<2–3 s) onto the rotating substrate to finish film deposition. For the perovskite films, compared to static spin-coating, several recent studies show that dynamic spin-coating can enhance the device performance. The successive loaded precursor solution during the dynamic spin-coating for perovskite film deposition helped with retaining the perovskite intermediate phase[35,36] and facilitated the cation ions intermixing.[37] As a result, high-quality perovskite films were obtained.

As for the HTL in PSCs, one of the most common materials combinations is $N^2,N^2,N2',N2',N7,N7,N7',N7'$-octakis(4-methoxyphenyl)-9,9'-spirobi[9H-fluorene]-2,2',7,7'-tetramine (Spiro-OMeTAD), 4-tert-butylpyridine (tBP), and lithium
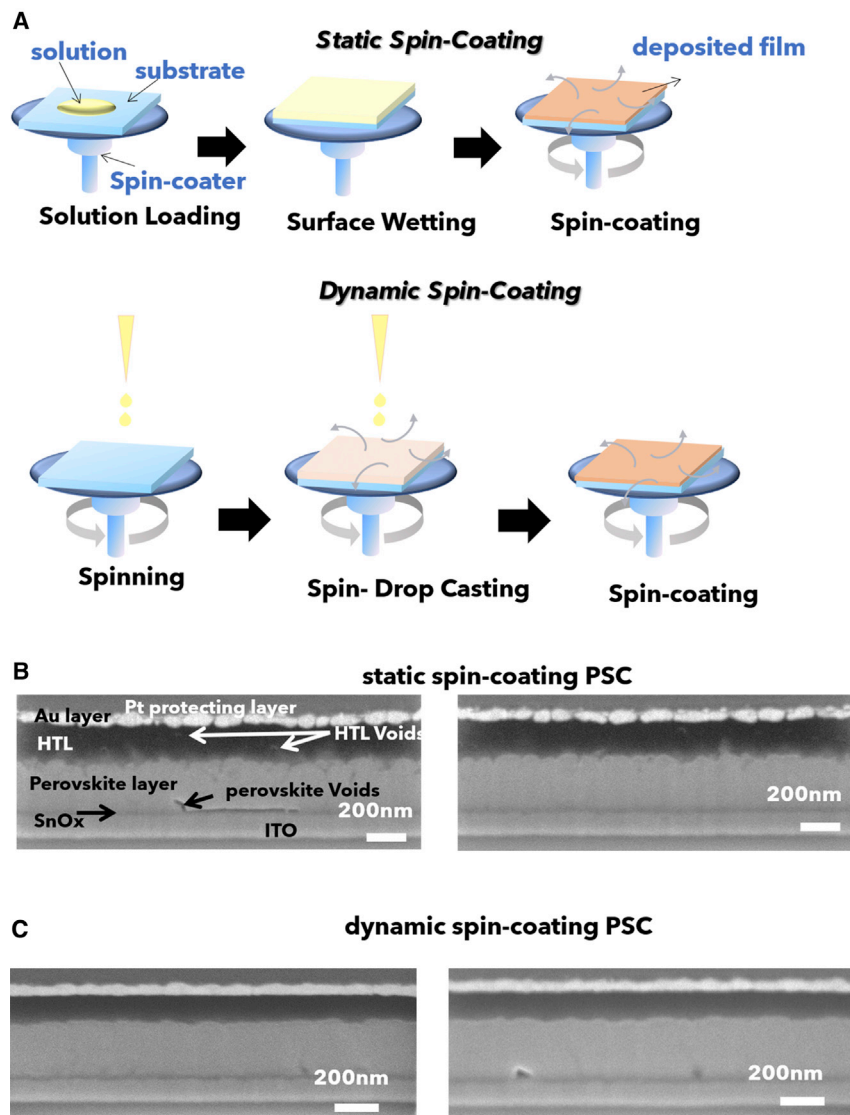
Figure 1. Perovskite Solar Cells for Which the HTLs Were Fabricated by Different Spin-Coating Methods

(A–C) Schematic representation of (A) static and dynamic spin-coating; cross-section FIB-SEM images at different locations for a PSC with HTLs deposited by (B) static spin-coating and (C) dynamic spin-coating.

bis(trifluoromethanesulfonyl)imide (LiTFSI). In this combination, Spiro-OMeTAD is the main hole transport material, LiTFSI is the Spiro-OMeTAD oxidizer to improve the hole mobility and conductivity,[38] and tBP is the layer's morphological controller, which can homogenize the LiTFSI distribution by forming the tBP-LiTFSI complexes.[33,39] Due to the low solubility of LiTFSI in chlorobenzene (solvent for the HTL), LiTFSI needs to be dissolved in acetonitrile first. The LiTFSI-acetonitrile solution, tBP, and Spiro-OMeTAD are dissolved in chlorobenzene together as the HTL solution. In previous literature, it has been reported that tBP and acetonitrile can dissolve PbI_2, which is the precursor for perovskite.[33,39,40] As a result, the perovskite layer can be damaged. To allay this concern in an n-i-p PSC, the HTL is usually deposited by dynamic spin-coating.[41] Thus, it is expected that the minimized direct

interaction time between tBP and acetonitrile to perovskite should alleviate the perovskite partially dissolved by the organics. However, the field lacks direct evidence to demonstrate this principle.

Due to the limited field of view, high-resolution 2D imaging may be unable to show the difference between the PSCs with an HTL deposited by static spin-coating (s-PSCs) and dynamic spin-coating (d-PSCs). As shown in Figure 1B, the two cross-section SEM images were acquired from the same s-PSC. The left image shows more voids in the perovskite layer than that of the right image. In Figure 1C, the two cross-section SEM images were acquired from the same d-PSC, which also displayed different morphology at perovskite layers. If comparing the left two images in Figures 1B and 1C, there are more perovskite layer voids in the s-PSC. In contrast, if comparing the right two images in Figures 1B and 1C, the opposite conclusion is drawn: there are more perovskite layer voids in the d-PSC. Such samples require 3D characterization to evaluate the difference between s-PSC and d-PSC voids and morphology.

In this research, FIB-SEM 3D reconstruction is applied to PSCs to observe their buried layers and interfaces. The 3D structures for s-PSC and d-PSC are reconstructed and compared at high resolution. It shows that the different HTL deposition methods have obvious impacts on the morphology of the perovskite layer, HTL, gold layer, and their interfaces. Additionally, liquid chromatography-mass spectrometry (LC-MS), angle-resolved X-ray photoelectron spectroscopy (AR-XPS), and ultraviolet photoelectron spectroscopy (UPS) are applied to characterize that the HTL spin-coating methods yielded different compositional ratios, interfacial structures, and energy levels of the HTLs and their associated interfaces. We propose a mechanism based on the precursors solubility difference in organic solvent to explain why these two film deposition methods lead to the obvious compositional and morphological differences. Collectively, this study suggests that the researchers need to carefully select the deposition methods to obtain the desired film composition and morphology. For the multi-components' HTL deposition in PSCs, this study demonstrates the dynamic spin-coating method is better than static spin-coating method.

RESULTS AND DISCUSSION

3D Reconstructions of PSCs

In this study, both s-PSCs and d-PSCs are planar structure devices. The device architecture consists of SnO_x electron transport layer, $CH_3NH_3PbI_3$ perovskite layer (with extra CH_3NH_2 as Lewis base additive), Spiro-OMeTAD HTL (with LiTFSI and tBP additives), and 80-nm gold layer.[42] Except for the HTLs, other layers in s-PSCs and d-PSCs have identical fabrication conditions. 20 devices for each condition had been measured (their efficiencies with forward scan and reverse scan were displayed in Figure S1). As shown in Figures 2A and S1 and Table S1, the J-V curve for d-PSC had higher efficiency (the efficiencies [reverse scan] for s-PSC and d-PSC are 15.6% and 18.2%, respectively) and less hysteresis than s-PSC. It indicated that, for HTL, dynamic spin-coating was superior to static spin-coating. However, as discussed before, just comparing the cross-section SEM images (Figure 1) could not explain why d-PSC is better than s-PSC. 3D morphological information is necessary for this case.

Figures S2A and S2B show the schematic and SEM images of a PSC for 3D reconstruction. The milling current for 3D reconstruction was limited to 5 pA at 30 kV. This meant that the Ga^+ ion dosage rate was much lower than conditions for normal
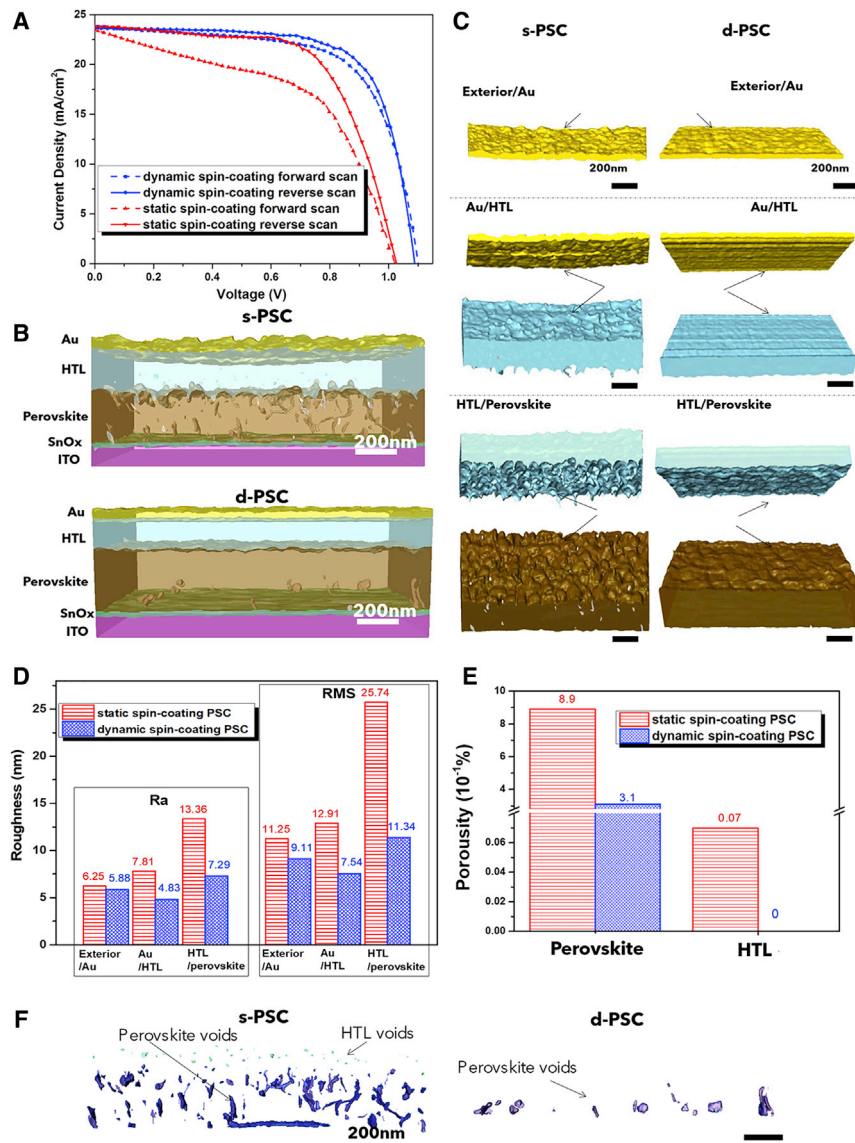
Figure 2. The 3D Reconstruction for the Layers and Interfaces in s-PSC and d-PSC

(A–F) s-PSC and d-PSC J-V curves (A); reconstructed 3D full device structures for s-PSC and d-PSC (B); morphology of the layers and interfaces in 3D reconstructed s-PSC and d-PSC (C); roughness results (average roughness [Ra] and root mean square [RMS]) for the interfaces in s-PSC and d-PSC (D); porosity results for the perovskite layer and HTL in s-PSC and d-PSC (E); and the 3D reconstructed HTL voids (light green) and perovskite voids (dark blue) in s-PSC and d-PSC (F).

FIB milling processes used to prepare cross-section images for PSCs.[38,43] This is expected to limit ion-beam-induced sample morphological change.[44]

FIB-SEM carries other benefits for PSCs imaging: the entire thickness for a typical PSC is within 3 μm (in cross-section view without counting the conductive substrate), which means that even a small FIB milling current (~pA) is enough to efficiently micro-machine the slices. In our experiments, the time for processing of all the slices and image acquisition was finished within 2 h—this was even shorter than the time for using FIB-SEM to prepare a PSC TEM lamella (~4.5–6 h).[33,38] In contrast, if a device has thick layers (>5 μm), FIB-SEM requires a longer acquisition time and larger

milling current (∼nA). In our previous research, the technique was applied for lithium metal anode. Due to the large film thickness and beam sensitivity of Li metal, the samples had to be milled at a cryogenic condition in order to minimize the large ion beam current-induced morphological change.[45,46] On the other hand, compared with other 3D reconstruction techniques, FIB-SEM also has obvious advantages: The cross-section image resolution for a FIB-SEM 3D reconstruction is the same as SEM. The resolution for FIB milling direction is 10 s of nanometer, which is limited by the thinning thickness. It means the majority of the morphological information in PSCs can be observed. TEM 3D reconstruction may show even higher resolution; however, due to the low beam stability for PSCs in TEM, the technique needs to be further developed to minimize the damaging effects.[44]

The 3D images were reconstructed in Thermo Scientific Avizo Software 2019.1. All functional layers and voids were labeled as shown in Figures S2C and S2D. After stacking all labeled slices together, the device 3D structures were obtained. Figure 2B displayed the FIB-SEM 3D reconstructed s-PSC and d-PSC. For checking the influence of HTL additive, the HTL additive-free s-PSC was also 3D reconstructed as shown in Figure S3A. Recall that it was hard to draw accurate conclusions from individual cross-section SEM images (Figure 1). In the FIB-SEM data, we clearly observed the morphological difference between the s-PSC and d-PSC (Figures 2B and S3A). Three videos demonstrate the process for FIB-SEM 3D reconstruction of the s-PSC (Video S1), d-PSC (Video S2), and HTL additive-free s-PSC (Video S3).

To compare the morphological differences for s-PSC and d-PSC, the roughness and porosity of the devices were calculated as shown in Figures 2C–2F (for detailed roughness information, see Tables S2 and S3). The morphologies of layers and interfaces for HTL additive-free s-PSC were displayed in Figures S3B–S3D. Two videos for the s-PSC and d-PSC show voids in between Au and ETL (Videos S4 and S5). The roughnesses of exterior/Au, Au/HTL, and HTL/perovskite interfaces for s-PCS are larger than d-PSC (Figures 2C and 2D). Especially for the HTL/perovskite interfaces, the Ra and root mean square (RMS) of s-PSC are almost twice that of d-PSC. This can be attributed to the fact that the dynamic spin-coating minimized the etching effects from tBP and acetonitrile in HTL solution to perovskite layer. During dynamic spin-coating, the fast spin-coating revolutions per minute enable the substrate to get rid of excess amount of tBP and acetonitrile immediately; as a result, the relative smooth perovskite film was protected. On the other hand, in s-PSC, the HTL solution needs to wet the perovskite substrate in order to cover the entire surface before spin-coating. During this period of time, the tBP and acetonitrile can partially dissolve the perovskite layer. Additionally, the perovskite porosity demonstrates d-PSC had fewer voids than s-PSC (Figures 2E and 2F). This could be explained for the same reason—the dynamic spin-coating can prevent the tBP and acetonitrile from etching the perovskite layer. Moreover, compared with the s-PSC, the HTL additive-free s-PSC in Figure S3 demonstrated less roughness at the HTL/perovskite interface. It further indicates the HTL additive etching is the main reason to cause the morphological change in s-PSC, although dynamic spin-coating can minimize this impact.

For comparison, top-view *ex situ* SEM images were taken (Figure S4) to compare the morphological differences between the perovskite layers with the HTL deposited by static or dynamic spin-coating. Before taking the top-view images of the buried perovskite layers, HTL should be removed first. For these experiments, finding a "proper" solvent was crucial. The solvent had to dissolve all HTL components
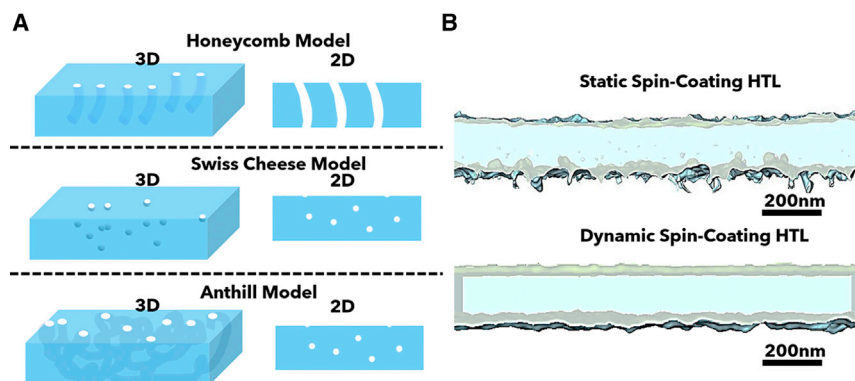
Figure 3. 3D HTL Morphology in PSCs
(A) Three proposed HTLs (with defects) models (honeycomb, Swiss cheese, and anthill models) with 3D and cross-section 2D structures.
(B) FIB-SEM 3D reconstructed HTLs in PSCs prepared by static spin-coating and dynamic spin-coating.

without dissolving the perovskite layer. After screening a series of organic solvents, only chloroform met this requirement. Other solvents either could not dissolve all HTL components (for instance, chlorobenzene cannot dissolve LiTFSI) or may partially dissolve perovskite layer (for instance, isopropanol), which had to be ruled out. However, even chloroform can change the morphology of perovskite film. As shown in Figures S4A and S4B, the morphology of a freshly prepared perovskite layer (Figure S4A) was changed after treatment with chloroform (Figure S4B). As a result, although in Figures S4C and S4D, the *ex situ* SEM of the perovskite films with the HTL deposited by dynamic spin-coating showed fewer pinholes than the static spin-coating sample, it cannot represent the actual perovskite film morphology. Chloroform had already changed the perovskite film morphology as an artifact. In contrast, in Figure 2C, the perovskite film from d-PSC demonstrates smooth and less pin-hole morphology, in which top surface is as similar as Figure S4A. We conclude that means the d-PSC perovskite film almost maintained the same morphology as a freshly prepared perovskite film. The comparison of perovskite film morphologies in Figures 2C and S2 exhibits the FIB-SEM 3D reconstruction has unique advantages for *in situ* characterizing the buried layers and interfaces in a device.

On the other hand, voids were observed in the s-PSC HTL although in the d-PSC was not (Figures 2E and 2F). It indicates that the tBP or acetonitrile etching to perovskite could be one of the factors on the formation of HTL voids. During the etching, bubbles may form in the HTL solution, and this manifests as voids in deposited HTL. As displayed in Figure 3A, previous research proposed two types of "imperfect" Spiro-OMeTAD HTL 3D structures. The first can be termed the "honeycomb model."[47–49] In this model, HTL has channel-like pinholes across the entire film without twisting. Moisture and oxygen can diffuse through the pinholes, thus serving as degradation sites for the perovskite layer. The pinhole origins were attributed to the HTL compositional migration, such as Li$^+$. This model was supported through top-view SPM. Another model can be termed as the "Swiss cheese model."[33] In this model, the bubble-like voids spread in the HTL. The formation of voids was ascribed to the tBP evaporation and LiTFSI enrichment. This model was evaluated by the cross-section FIB-TEM. The 2D cross-section FIB-TEM may differentiate the honeycomb and Swiss cheese models by observing the HTL morphology in a high resolution. As Figure 3A displayed, if the honeycomb model is correct, because the pinholes cross the

entire HTL to connect to perovskite without twisting, the channel-like structures in HTL will be observed by FIB-TEM. On the other hand, if the bubble-like structures were observed in HTL, Swiss cheese model could be correct. However, in Figure 3A, there is also a third possibility: if the pinholes in HTL are twisted as coils, the similar morphology should be observed as the Swiss cheese model in the 2D cross-section FIB-TEM. The HTL with twisted pinholes across the HTL can be termed as the "anthill model." With the help of 3D reconstruction, the accurate HTL 3D model is able to be observed. As displayed in Figure 3B, the dynamic spin-coating HTL has a dense and void-free film. Regarding the static spin-coating HTL, only the bubble-like voids exist in the HTL, and the actual 3D structure for the imperfect HTL in PSC agrees with the Swiss cheese model.

The 3D reconstructions for s-PSC and d-PSC demonstrated obvious morphological differences on their functional layers and interfaces. To understand why different HTL spin-coating methods can show huge impacts on the devices morphology, several characterizations were applied to probe the compositional information of the HTLs.

Compositional and Energy Band Differences in HTLs

To understanding why HTL spin-coating methods could influence the morphology of PSCs, several characterizations were applied to compare the differences between the HTLs. First the film thicknesses prepared at different revolutions per minute were measured (deposition time was 20 s; the revolutions per minute ranged from 500 to 5,000). As shown in Figure 4A, almost all static spin-coating HTLs had larger film thicknesses than the dynamic spin-coating samples. The SEM and 3D reconstruction results in Figures 1B, 1C, and 2B also display the same phenomena that the s-PSC has a thicker HTL than d-PSC. It can be attributed to a process where successive liquid droplets during the dynamic spin-coating may re-dissolve the deposited materials on the films.

In the meantime, the HTLs' compositional ratios were characterized by high-performance liquid chromatography-MS (HPLC-MS). The results were summarized in Figure 4B. More detailed information for the HPLC-MS results were shown in Figure S5 and Table S4. As a reference, the solution composition for HTL spin-coating has a 4:2:1 tBP:Spiro-OMeTAD:LiTFSI molar ratio. According to Figure 4B and Table S4, both of the films have higher LiTFSI:tBP and LiTFSI:Spiro-OMeTAD ratios than the precursor solution. The tBP:Spiro-OMeTAD:LiTFSI ratios are 0.75:0.75:1 for static spin-coating HTL and 0.6:0.6:1 for dynamic spin-coating HTL. It means that the LiTFSI was enriched during the spin-coating process. The dynamic spin-coating HTL has even higher LiTFSI ratio than that of the static spin-coating HTL. This trend has been further evidenced by the HTLs energy diagram. As shown in Figures 4C and 4D, the valence band, work function, and band gap for the HTLs deposited by different spin-coating methods were characterized by ultraviolet spectroscopy (UPS) (22.12 eV HeI source) and Tauc-Plot UV-Vis. To rule out the influence of Spiro-OMeTAD oxidation reaction, the films were deposited in Ar environment glove box and transferred to UPS by an N_2 environment glove box. The energy band diagram based on Figures 4C and 4D were displayed in Figure 4E. It shows that the valence band for dynamic spin-coating HTL is more close to Fermi level, which indicates this film has been more p-doped than the static spin-coating HTL. Previous researches reported LiTFSI is the p-dopant in Spiro-OMeTAD-based HTL.[38,50] Without obviously changing the band gap (Figure 4D), the results in Figure 4E agree with the HPLC-MS results that the dynamic spin-coating HTL has higher LiTFSI ratio than static spin-coating HTL.
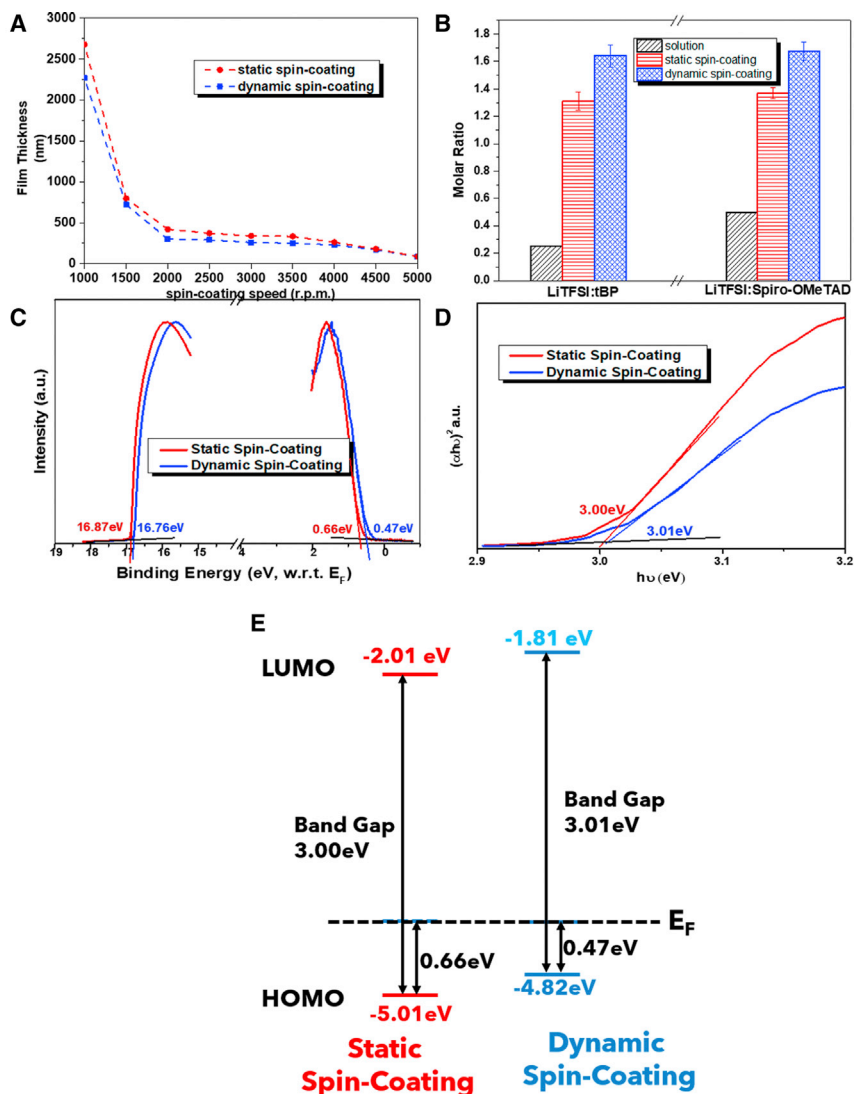
Figure 4. Composition and Band Structures for Static and Dynamic Spin-Coating HTLs

(A–E) HTL film thickness at different spin-coating speeds (A); compositional molar ratio derived from liquid chromatography-mass spectrometry (the solution for spin-coating were displayed as a reference and the error bars represent the HPLC of 3 independent replicates for each sample; B); ultraviolet photoelectron spectroscopy (C); Tauc-Plot UV-Vis (D); and energy band diagram (E). The HTL films in (B)–(E) were spin-coated at 4,000 rpm, which were the same conditions for the HTLs in PSCs.

As discussed before, the tBP:Spiro-OMeTAD:LiTFSI molar ratio in solution is changed from 4:2:1 to 0.75:0.75:1 (static spin-coating HTL) or 0.6:0.6:1 (dynamic spin-coating HTL) after film deposition. Compared to the precursor solution, this ratio change illustrated that the deposited films have materials loss and the loss order is tBP > Spiro-OMeTAD > LiTFSI. Moreover, the dynamic spin-coating sample has more materials loss than the static spin-coating sample. On the other hand, the material's loss order is the same as the HTL components' solubility in chlorobenzene, which is the solvent for HTL solution. In chlorobenzene, as a liquid component, tBP was miscible with the solvent, although Spiro-OMeTAD was soluble. However, LiTFSI has less solubility in chlorobenzene, and its dissolving process in chlorobenzene required acetonitrile and tBP. LiTFSI was dissolved in acetonitrile first (the LiTFSI-acetonitrile solution was shown
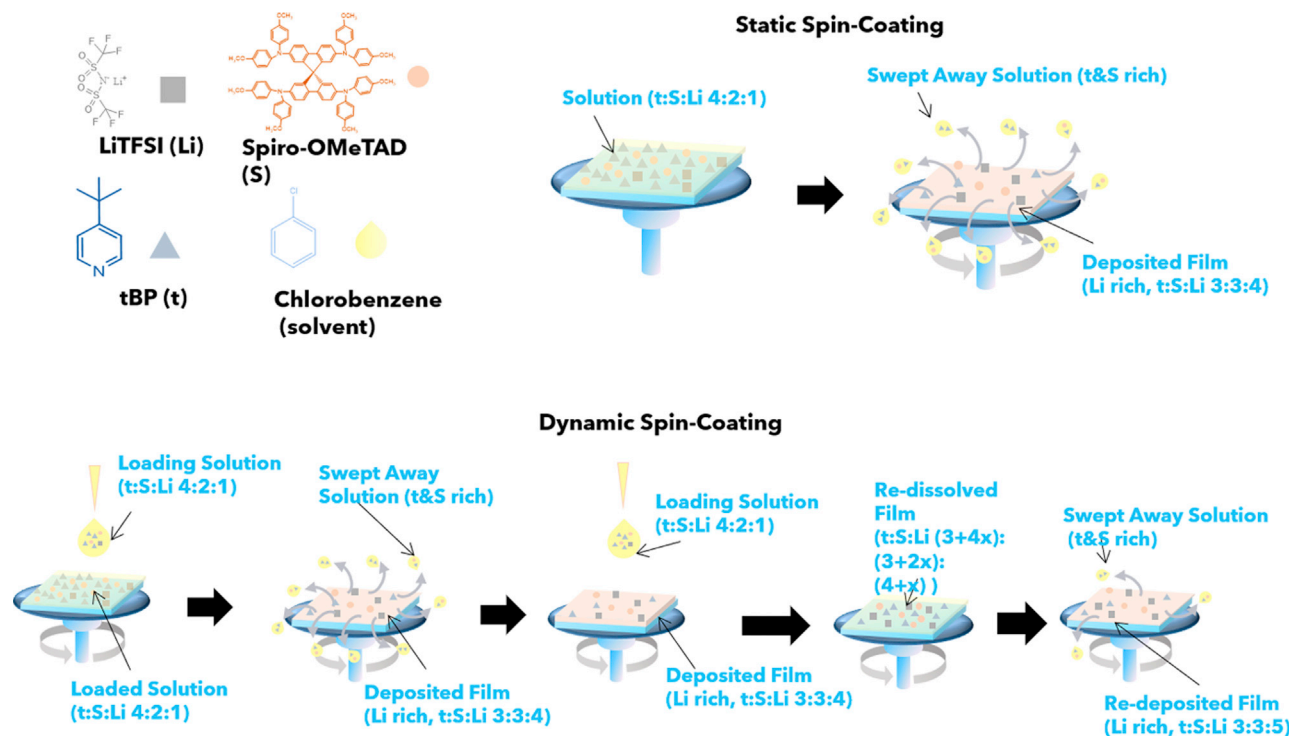
Figure 5. Proposed Mechanism for the Compositional Differences in Static and Dynamic Spin-Coating HTLs

Before spin-coating, the compositional molar ratio in the precursor solution is tBP:Spiro-OMeTAD:LiTFSI 4:2:1 (chlorobenzene as solvent). After deposition, the tBP:Spiro-OMeTAD:LiTFSI molar ratio changed as 3:3:4 for static spin-coating HTL and 3:3:5 for dynamic spin-coating HTL.

as visibly blurred liquid droplets in chloroform). After adding tBP, the formation of tBP-LiTFSI complexes can finally help LiTFSI to be homogenized dissolving in chlorobenzene.[33,39] So in general, the HTL components' solubility in chlorobenzene is tBP > Spiro-OMeTAD > LiTFSI. It indicates that the compositional changes in these deposited films may be induced by the materials' solubility difference in chlorobenzene. Furthermore, tBP, as the only volatile liquid component, can decrease even more due to the evaporation during spin-coating.

Based on these observations and concerns, a mechanism was proposed in Figure 5 to demonstrate the compositional difference of the HTLs deposited by different spin-coating methods: in the static spin-coating case, the wetted substrate contains 4:2:1 molar ratio of tBP, Spiro-OMeTAD, and LiTFSI in chlorobenzene. During the spin-coating, the solution liquid droplets, which are rich in tBP and Spiro-OMeTAD, will be swept out of the substrate. Due to the low solubility in chlorobenzene, compared to tBP and Spiro-OMeTAD, less LiTFSI will be swept out of the substrate. As a result, the ratio of LiTFSI is much higher on the deposited film with respect to tBP and Spiro-OMeTAD. As for the dynamic spin-coating HTL, the liquid droplets are continuously loaded onto the substrate in the first several seconds while the substrate is spinning. During the process, the earlier loaded solution droplets have formed as film, which has higher LiTFSI ratio. However, the later loaded solution droplets can re-dissolve the film and swept away the tBP- and Spiro-OMeTAD-rich droplets. Less of LiTFSI in the film will be re-dissolved for its low solubility in chlorobenzene. The re-dissolved tBP and Spiro-OMeTAD will be swept away with even less amount remaining on the film. As a result, the dynamic spin-coating HTL has even higher LiTFSI molar ratio, due to the initial-deposited film are re-dissolved by the
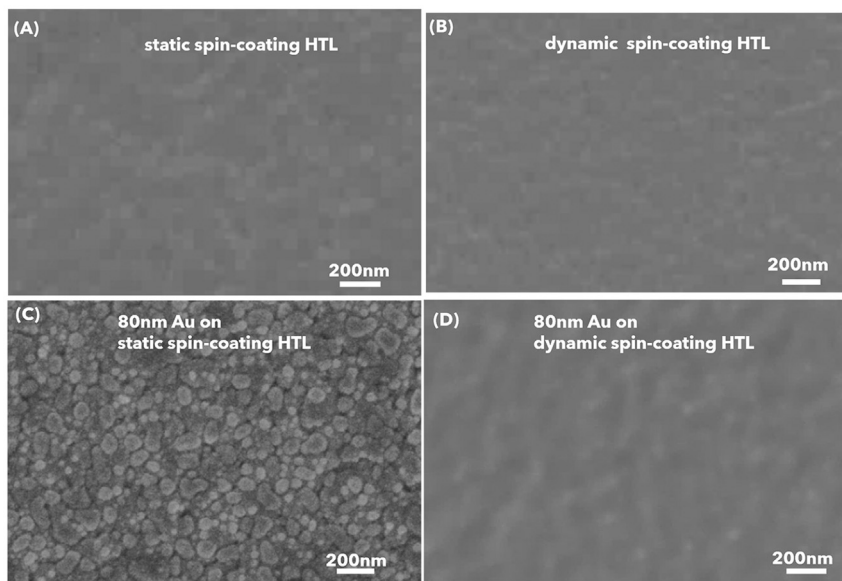
Figure 6. SEM Top-View SEM Images for the Samples that HTL Deposited by Different Spin-Coating Methods

(A–D) HTL deposited by (A) static spin-coating and (B) dynamic spin-coating; 80 nm Au deposited on (C) static spin-coating HTL and (D) dynamic spin-coating HTL.

successive loaded solution. This re-dissolved process also is confirmed by Figure 4A, which indicates that the dynamic spin-coating HTL has less film thickness than static spin-coating HTL.

The proposed mechanism in Figure 5 is able to explain the compositional differences of the HTL, which deposited by different spin-coating methods. Moreover, the roughness and porosity differences for s-PSC and d-PSC on the HTL, perovskite, and HTL/perovskite interface had been attributed to the etching effect from tBP and acetonitrile to perovskite. However, according to Figures 2C and 2D, the exterior/Au and Au/HTL interface for s-PSC and d-PSC also demonstrate different roughness and morphology. Regarding these two interfaces, the s-PSC also has larger surface roughness than d-PSC. So next, the difference for s-PSC and d-PSC's Au layer (exterior/Au interface) and Au/HTL interfaces will be discussed.

Au Layer (Au/Exterior Interface) and Au/HTL Interface in PSCs

According to Figures 6A and 6B, the top-view SEM images indicate that there is almost no obvious morphological difference between the top surfaces of static and dynamic spin-coating HTL. The morphological change happens after Au deposition. As Figures 6C and 6D displayed, the Au on dynamic spin-coating HTL maintains the similar morphology of the HTL, whereas the Au has island-like structures on the static spin-coating HTL. It agrees with the 3D reconstruction results in Figures 2C–2F. The Au layers in Figures 6C and 6D were deposited together. Moreover, the instrument is equipped with a cooling system to keep the substrate at 20°C during the deposition. Therefore, the Au difference for s-PSC and d-PSC should not be attributed to the thermal-induced effect.

To investigate the reason for the Au morphological difference, angle-resolved XPS (AR-XPS) was applied to investigate the Au/HTL interfaces in s-PSC and d-PSC. As

shown in Figure 7A, 5 nm of Au was deposited on these HTLs before the characterization to ensure the HTL buried interface could be detected by AR-XPS because the maximum probing depth in XPS is ~10 nm. Each sample was tilted at 0° and 60° take-off angles, respectively. In AR-XPS, the maximum probing depth is $3\lambda\cos\theta$, where the θ is take-off angle and λ is the materials electrons inelastic mean free path. At 0°, all compositional information is the same as normal XPS. For minimizing to collect the elastic scattering electrons from deeper thickness in AR-XPS, the largest tilting angle for the experiments was restricted to 60°, though the instrument (AXIS-Supra) can be tilted to even a higher angle (80°).[51] When tilting at 60°, the maximum probing depth is ~5 nm, which means the compositional information is more close to the Au/HTL interface. The survey spectra (all peaks were labeled) and XPS spectra of N 1s, O 1s, and S 2p were displayed in Figures S6 and S7. It has to note that, though the samples contain LiTFSI, the Li signal cannot be detected due to the low relative sensitive factor of Li 1 s peak, and also, the peak is overlapping with Au 5p.

In Figure 7B, for both samples the F 1s AR-XPS spectra have two components, $TFSI^-$ at 688.7 eV and F^- at 685.2 eV. It had been reported that the F^- might from the X-ray-induced $TFSI^-$ decomposition.[47] A controlled XPS experiment was conducted for the HTL sample, which measured over 10 times. As displayed in Figure S8, the Spiro-OMeTAD-based HTL has a "fluoride testing window": within 5 times measurements in our condition, the F^- amount was not changed. After that, a linear positive correlation was observed between the F^- amount and the XPS measurement time that indicates the X-ray-induced $TFSI^-$ decomposition happened. It means that the F^- is the intrinsic component in the HTL if the measurements controlled within 5 times, and the all AR-XPS results in this study meet the requirements. Under this concern, within the F testing window, the formation of F^- in HTL can be attributed to the partial decomposition of LiTFSI during the HTL spin-coating. As shown in Figure 7B, both HTLs have more F^- components when close to the Au/HTL interface because the 60° AR-XPS results have higher F^- ratio. From the bulk to Au/HTL interface, the HTL that deposited by dynamic spin-coating has a steeper F^- change (from bulk to surface, 4.6%–25.4%) than static spin-coating (from bulk to surface, 12.7%–33.6%). On the contrary, in Figure 7C, the C 1s spectra display the opposite trends. In the spectra, the ratio of sp^2 carbon (C=C) at 283.8 eV to sp^3 carbon (C–H and C–C) at 284.6 eV can be applied for evaluating the Spiro-OMeTAD oxidation. It is because the oxidized Spiro-OMeTAD has fewer π electrons than the pristine one. The higher of (C–H and C–C):(C=C) ratio means the more oxidized Spiro-OMeTAD exists. In Figure 7C, from the bulk to surface, the (C–H and C–C):(C=C) ratio for static spin-coating HTL changed from 0.29 to 1.44, although the values change for dynamic spin-coating HTL is from 0.89 to 1.36. It means the oxidized and pristine Spiro-OMeTAD is more uniform distributed in the dynamic spin-coating HTL.

The AR-XPS C1s and F 1s spectra indicate that the dynamic spin-coating HTL has a more steep distribution of F components and uniform distribution of the oxidized and pristine Spiro-OMeTAD than that of static spin-coating HTL. This could be attributed to that the dynamic spin-coating sample has the components re-dissolve process and LiTFSI enrichment during the spin-coating. As a result, all species gradient had been changed and remixed, although some of the $TFSI^-$ enriched on the surface and decomposed as F^-.

To further observe the Au/HTL interface for the HTLs, the components' distribution was reconstructed by comparing the value $\ln(I_{60°}/I_{0°})$ for each component in the AR-XPS.[52] I_{degree} is the intensity of the components in AR-XPS at certain degree. A relative depth plot image can be obtained by comparing these values as shown in
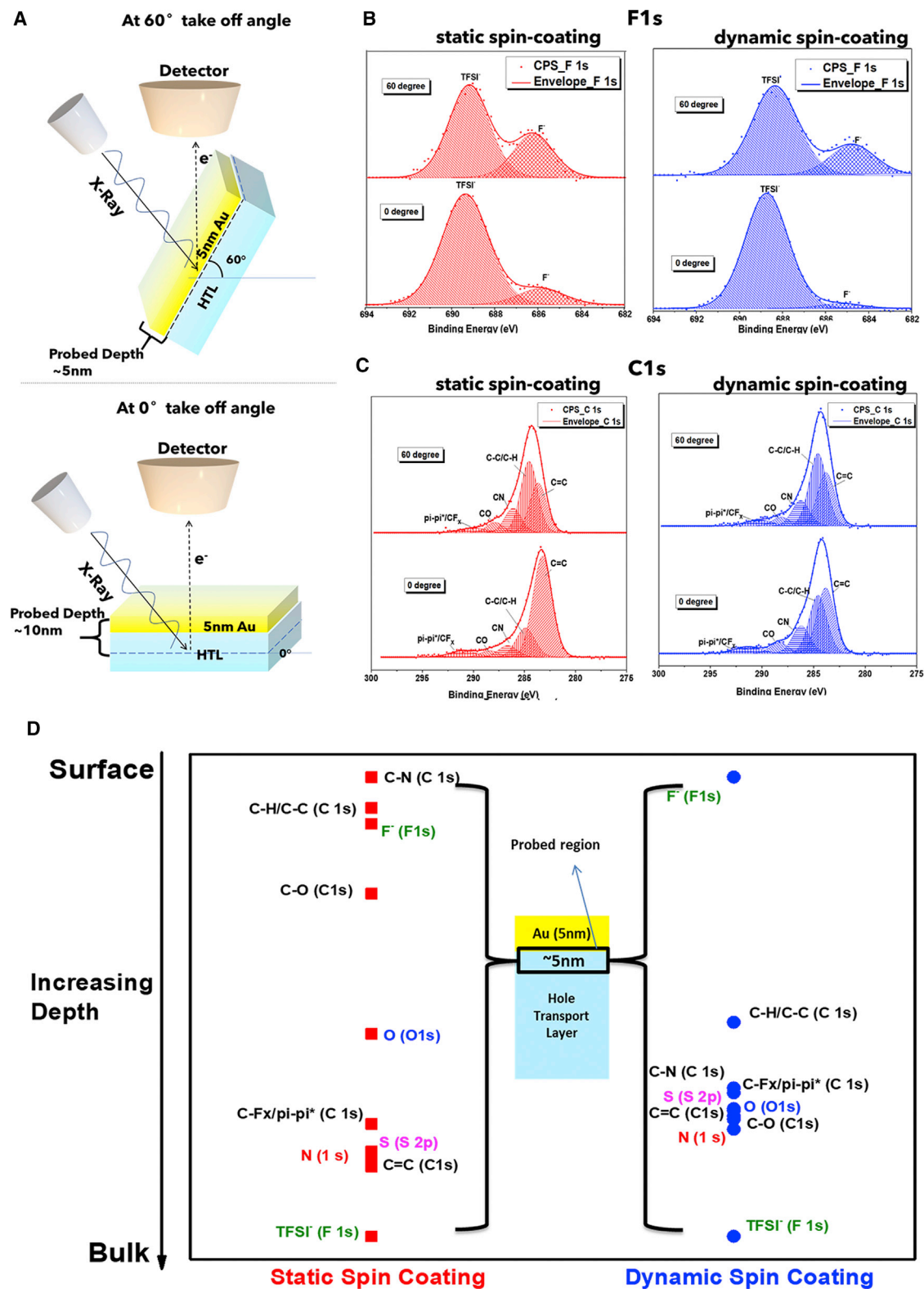
Figure 7. Angle-Resolved X-Ray Photoelectron Spectra

(A–D)AR-XPS at 0° and 60° take-off angles with Al Kα anode source (1,486.6 eV) for the HTLs coated with 5 nm Au: (A) a schematic illustrates the AR-XPS experiments for Au (5 nm)-coated HTL samples at 0° and 60° take-off angles, (B) F 1 s, (C) C 1 s, and (D) relative depth plot of the HTLs chemical components at Au/HTL interfaces. The results were derived from AR-XPS at 0° and 60° taking-off angles.

Figure 7D. In the relative depth plot results, the static spin-coating sample has more widespread data points, which indicates the components have gradient distribution. Moreover, the organic species, such as CN, C–H, and C–C in static spin-coating sample are on top of F^-; during the gold deposition, the Au vapor might embed with these components and result in a higher roughness Au layer. In dynamic spin-coating HTL, F^- is located at the top surface of the HTL. The inorganic component might be able to prevent the Au diffused into the HTL during the e-beam evaporation. As a result, the morphology of Au was the same as the HTL without deposition as the 3D reconstruction results (Figure 2) and SEM images (Figure 6) displayed. In general, the dynamic spin-coating changed the components' distribution in HTL, which enables the HTL to maintain its roughness during the Au deposition.

In summary, FIB-SEM 3D reconstruction was applied for unveiling the buried layers and interfaces in perovskite solar cells at high resolution. With the help of the technique, two types of PSCs were compared into which HTLs had been deposited by static and dynamic spin-coating. Both devices' buried interfaces and layers were able to be imaged by the 3D reconstruction and showed different surface roughness and porosity. The roughness changes on HTL/perovskite interfaces were attributed to the etching effect of the HTL components. In HTL, the 3D reconstruction results suggest the Swiss cheese model could be the right structure for the HTL with defects. The compositional differences for the HTLs prepared by different spin-coating methods were investigated by HPLC-MS. It suggests that the dynamic spin-coating method can enrich LiTFSI in the HTL. A mechanism was proposed to explain why the spin-coating methods can lead to the compositional ratio change in HTL. It indicates that the solubility for each component in the HTL solvent and the re-dissolve during dynamic spin-coating results in the difference. The 3D reconstruction results also displayed the morphological difference on Au/HTL and exterior/Au interfaces between the two spin-coating methods. It was further characterized by the AR-XPS, which demonstrates the different spin-coating methods can change the concentration gradient for each component on the Au/HTL interface. The dynamic spin-coating HTL has a "firm" interface to resist the morphological change from the Au deposition. Researchers may pay attention to choose "right" spin-coating methods once the precursor solution contains multiple components that have different solubility in the spin-coating solvent. These results also suggest 3D reconstruction by FIB-SEM can be a versatile and indispensable technique for perovskite device characterizations, especially for the morphological information of buried layers and interfaces.

EXPERIMENTAL PROCEDURES

Resource Availability

Lead Contact

Information and requests for resources and materials should be directed to the lead contact, Ying Shirley Meng (shirleymeng@ucsd.edu).

Materials Availability

Materials synthesized in this manuscript can be obtained by request to the lead contact.

Data and Code Availability

The published article includes all datasets generated or analyzed during this study.

Materials

All reagents, unless otherwise specified, were purchased from Sigma-Aldrich.

Perovskite Solar Cells Fabrication

The devices were fabricated in a fume hood at ambient condition.

The PSC has an n-i-p planar architecture, with ITO Glass/SnO$_x$/CH$_3$NH$_3$PbI$_3$/doped Spiro-OMeTAD/Au. The ITO (indium-doped tin oxide) glass slides were cut to 5 cm^2 (2 cm by 2.5 cm). The slides were etched by Zn powder with HCl with a 1 cm by 2 cm area to prevent short circuiting. They were cleaned by ultrasonication in 2% Hellmanex solution (in water), deionized water, isopropanol, and acetone, sequentially for 15 min. After drying the substrates and with 10-min oxygen plasma treatment, the slides were ready for materials deposition.

0.1M SnCl$_2 \cdot$ 2H$_2$O-ethanol solution was spin-coated at 2,000 rpm for 30 s on the substrates and annealed at 180°C for 1 h to form the SnO$_x$ layer.

Before perovskite deposition, the films were treated by oxygen plasma for 15 min. The perovskite solution contains equimolar (1.5 M) of CH$_3$NH$_3$I and PbI$_2$ in DMSO-DMF (1:9 volume ratio) solvent with 3% volume of CH$_3$NH$_2$-EtOH solution. The solution was stirred and heated at 75°C overnight. The films were spin-coated with the solution at 2,000 rpm for 25 s and followed by 1 mL of ethyl ether drop casted as the anti-solvent within 7 s at 3,000 rpm.

The HTL solution contains 17.7 μL LiTFSI-acetonitrile (520 mg/mL) solution, 20 μL tBP, and 0.08 g Spiro-OMeTAD (Merck) in 1 mL chlorobenzene solvent. The solution was prepared in an Ar environment glove box with a <0.1 ppm water level. For static spin-coating HTL, 80 μL of HTL solution was spread on the substrate before starting spin-coating. Then, the films were spin-coated at 4,000 rpm for 20 s. For dynamic spin-coating HTL, 80 μL of HTL solution was loaded within the first 2 s once the substrate started spinning at 4,000 rpm, the entire spin-coating time is 25 s.

80 nm of Au was deposited on the devices by e-beam evaporator.

Perovskite Solar Cells 3D Reconstruction

For 3D reconstruction, the data acquiring is an automatic process in FIB-SEM (FEI Scios DualBeam FIB-SEM). As shown in Figure 2B, in the experiment, a 5 μm by 5 μm Pt protective layer was deposited first in FIB-SEM, with a 500-nm thickness to prevent the sample damaged by ion beam. After that, three sides (front [8 μm × 2 μm × 5 μm], left and right [3 μm × 10 μm × 5 μm]) around the Pt layer were milled to ensure the acquired region is distinguishable. A fiducial marker with an "X" shape (2 μm × 500 nm × 500 nm) was milled near the image acquisition region for the software (Auto Slice and View) to identify the proper position. During the image acquisition process, the software can automatically mill, focus, and take image for each slice at the assigned cross-section region sequentially. For each device, 40 slices (30-nm thickness for each slice) were acquired along with the red arrow in Figure 2B. The FIB milling current is 5 pA at 30 kV, and the SEM imaging current is 0.1 nA at 5 kV.

After acquiring all slices of images in FIB-SEM, the results were reconstructed in Thermo Scientific Avizo Software 2019.1. All functional layers and voids in the software were labeled as shown in Figures S1A and S1B. To measure roughness, we measured deviation in Z from the median of a layer's minimum and maximum height in Z for every XY coordinate. The distances were calculated from surfaces calculated from segmentation data acquired through the segmentation editor after a non-local means filter on the raw data. Voids were omitted (by digitally filling them in) for

surface roughness calculations. Surface roughness calculations were calculated per interface and per device in Excel.

Characterization

The performances of PSCs were tested with a solar simulator with a 150 W xenon lamp (Solar Light SL07265; equipped with an AM1.5G filter; calibrated with a standard Si solar cell to simulate AM1.5 illumination [100 mW cm^{-2}]) and a Keithley 2400 source meter.

SEM images were taken by FEI Scios DualBeam FIB-SEM; the current is 0.1 nA at 5 kV.

Angle-resolved X-ray photoelectron spectroscopy (AR-XPS) and ultraviolet photoelectron spectroscopy (UPS) were performed using a Kratos AXIS Supra with Al Kα anode source (1,486.6 eV) operated at 15 kV and 10^{-8} Torr chamber pressure. The data were calibrated with the hydrocarbon C1s peak (284.8 eV) and processed by CasaXPS. In AR-XPS, the samples were coated with 5-nm thickness of Au and were measured at 0° and 60°.

UV-Vis spectra were carried out in an absorption mode on a Lambda 1050 UV-Vis spectrometer.

High-performance liquid chromatography-mass spectrometry was carried out in Thermo LCQdeca; 10 slides of spin-coated HTLs on 5 cm^2 ITO substrates in each condition were dissolved by chloroform to minimize the sample errors.

The porosity and roughness for the 3D reconstruction PSCs were calculated by Avizo.

SUPPLEMENTAL INFORMATION

Supplemental Information can be found online at https://doi.org/10.1016/j.xcrp.2020.100103.

AUTHOR CONTRIBUTIONS

S.W. conceived the idea, designed the experiments, and conducted most of the characterizations. A.C. helped with HPLC-MS, measured the film thickness, and collected the top-view SEM images. Y.Y. helped with the 3D reconstructions. S.V. performed the UV-Vis. A.S.H. did the structures' roughness calculation. Y.L. and J.-P.C.-B. demonstrated the different HTL preparation methods. M.K., Ø.F., and

D.P.F. helped with the results discussion. S.W. and Y.S.M. analyzed the data together. All authors discussed the results and commented on the manuscript. The manuscript was written through contributions of all authors. All authors have given approval to the final version of the manuscript.

DECLARATION OF INTERESTS

The authors declare no competing interests.

REFERENCES

1. Kojima, A., Teshima, K., Shirai, Y., and Miyasaka, T. (2009). Organometal halide perovskites as visible-light sensitizers for photovoltaic cells. J. Am. Chem. Soc. 131, 6050–6051.

2. Kim, H.S., Lee, C.R., Im, J.H., Lee, K.B., Moehl, T., Marchioro, A., Moon, S.J., Humphry-Baker, R., Yum, J.H., Moser, J.E., et al. (2012). Lead iodide perovskite sensitized all-solid-state submicron thin film mesoscopic solar cell with efficiency exceeding 9%. Sci. Rep. 2, 591.

3. Liu, M., Johnston, M.B., and Snaith, H.J. (2013). Efficient planar heterojunction perovskite solar cells by vapour deposition. Nature 501, 395–398.

4. Ball, J.M., Lee, M.M., Hey, A., and Snaith, H.J. (2013). Low-temperature processed meso-superstructured to thin-film perovskite solar cells. Energy Environ. Sci. 6, 1739–1743.

5. Lee, M.M., Teuscher, J., Miyasaka, T., Murakami, T.N., and Snaith, H.J. (2012). Efficient hybrid solar cells based on meso-superstructured organometal halide perovskites. Science 338, 643–647.

6. Park, N.G. (2015). Perovskite solar cells: an emerging photovoltaic technology. Mater. Today 18, 65–72.

7. Im, J.H., Lee, C.R., Lee, J.W., Park, S.W., and Park, N.G. (2011). 6.5% efficient perovskite quantum-dot-sensitized solar cell. Nanoscale 3, 4088–4093.

8. National Renewable Energy Laboratory (2020). Best research cell efficiencies. https://www.nrel.gov/pv/cell-efficiency.html.

9. Jung, E.H., Jeon, N.J., Park, E.Y., Moon, C.S., Shin, T.J., Yang, T.Y., Noh, J.H., and Seo, J. (2019). Efficient, stable and scalable perovskite solar cells using poly(3-hexylthiophene). Nature 567, 511–515.

10. Jiang, Q., Zhao, Y., Zhang, X., Yang, X., Chen, Y., Chu, Z., Ye, Q., Li, X., Yin, Z., and You, J. (2019). Surface passivation of perovskite film for efficient solar cells. Nat. Photonics 13, 460–466.

11. Wei, H., Fang, Y., Mulligan, P., Chuirazzi, W., Fang, H.H., Wang, C., Ecker, B.R., Gao, Y., Loi, M.A., Cao, L., et al. (2016). Sensitive X-ray detectors made of methylammonium lead tribromide perovskite single crystals. Nat. Photonics 10, 333–339.

12. Wei, W., Zhang, Y., Xu, Q., Wei, H., Fang, Y., Wang, Q., Deng, Y., Li, T., Gruverman, A., Cao, L., et al. (2017). Monolithic integration of hybrid perovskite single crystals with heterogenous substrate for highly sensitive X-ray imaging. Nat. Photonics 11, 315–321.

13. Wei, H., DeSantis, D., Wei, W., Deng, Y., Guo, D., Savenije, T.J., Cao, L., and Huang, J. (2017). Dopant compensation in alloyed $CH_3NH_3PbBr_{3-x}Cl_x$ perovskite single crystals for gamma-ray spectroscopy. Nat. Mater. 16, 826–833.

14. Lin, K., Xing, J., Quan, L.N., de Arquer, F.P.G., Gong, X., Lu, J., Xie, L., Zhao, W., Zhang, D., Yan, C., et al. (2018). Perovskite light-emitting diodes with external quantum efficiency exceeding 20 per cent. Nature 562, 245–248.

15. Cao, Y., Wang, N., Tian, H., Guo, J., Wei, Y., Chen, H., Miao, Y., Zou, W., Pan, K., He, Y., et al. (2018). Perovskite light-emitting diodes based on spontaneously formed submicrometre-scale structures. Nature 562, 249–253.

16. Wang, N., Cheng, L., Ge, R., Zhang, S., Miao, Y., Zou, W., Yi, C., Sun, Y., Cao, Y., Yang, R., et al. (2016). Perovskite light-emitting diodes based on solution-processed self-organized multiple quantum wells. Nat. Photonics 10, 699–704.

17. Lin, J., Lai, M., Dou, L., Kley, C.S., Chen, H., Peng, F., Sun, J., Lu, D., Hawks, S.A., Xie, C., et al. (2018). Thermochromic halide perovskite solar cells. Nat. Mater. 17, 261–267.

18. Wang, R., Mujahid, M., Duan, Y., Wang, Z.K., Xue, J., and Yang, Y. (2019). A review of perovskites solar cell stability. Adv. Funct. Mater. 29, 1808843.

19. deQuilettes, D.W., Vorpahl, S.M., Stranks, S.D., Nagaoka, H., Eperon, G.E., Ziffer, M.E., Snaith, H.J., and Ginger, D.S. (2015). Solar cells. Impact of microstructure on local carrier lifetime in perovskite solar cells. Science 348, 683–686.

20. Fu, K., Nelson, C.T., Scott, M.C., Minor, A., Mathews, N., and Wong, L.H. (2016). Influence of void-free perovskite capping layer on the charge recombination process in high performance $CH_3NH_3PbI_3$ perovskite solar cells. Nanoscale 8, 4181–4193.

21. Stranks, S.D., Eperon, G.E., Grancini, G., Menelaou, C., Alcocer, M.J.P., Leijtens, T., Herz, L.M., Petrozza, A., and Snaith, H.J. (2013). Electron-hole diffusion lengths exceeding 1 micrometer in an organometal trihalide perovskite absorber. Science 342, 341–344.

22. Jung, H.J., Kim, D., Kim, S., Park, J., Dravid, V.P., and Shin, B. (2018). Stability of halide perovskite solar cell devices: in situ observation of oxygen diffusion under biasing. Adv. Mater. 30, e1802769.

23. Nanova, D., Kast, A.K., Pfannmöller, M., Müller, C., Veith, L., Wacker, I., Agari, M., Hermes, W., Erk, P., Kowalsky, W., et al. (2014). Unraveling the nanoscale morphologies of mesoporous perovskite solar cells and their correlation to device performance. Nano Lett. 14, 2735–2740.

24. Kosasih, F.U., and Ducati, C. (2018). Characterising degradation of perovskite solar cells through in-situ and operando electron microscopy. Nano Energy 47, 243–256.

25. Zhang, D., Zhu, Y., Liu, L., Ying, X., Hsiung, C.E., Sougrat, R., Li, K., and Han, Y. (2018). Atomic-resolution transmission electron microscopy of electron beam-sensitive crystalline materials. Science 359, 675–679.

26. Divitini, G., Cacovich, S., Matteocci, F., Cinà, L., Di Carlo, A., and Ducati, C. (2016). In situ observation of heat-induced degradation of perovskite solar cells. Nat. Energy 1, 15012.

27. Luo, Y., Khoram, P., Brittman, S., Zhu, Z., Lai, B., Ong, S.P., Garnett, E.C., and Fenning, D.P. (2017). Direct observation of halide migration and its effect on the photoluminescence of methylammonium lead bromide perovskite single crystals. Adv. Mater. 29, 1703451.

28. Bergmann, V.W., Weber, S.A., Javier Ramos, F., Nazeeruddin, M.K., Grätzel, M., Li, D., Domanski, A.L., Lieberwirth, I., Ahmad, S., and Berger, R. (2014). Real-space observation of unbalanced charge distribution inside a perovskite-sensitized solar cell. Nat. Commun. 5, 5001.

29. Edri, E., Kirmayer, S., Henning, A., Mukhopadhyay, S., Gartsman, K., Rosenwaks, Y., Hodes, G., and Cahen, D. (2014). Why lead methylammonium tri-iodide perovskite-based solar cells require a mesoporous electron transporting scaffold (but not necessarily a hole conductor). Nano Lett. 14, 1000–1004.

30. Correa-Baena, J.P., Luo, Y., Brenner, T.M., Snaider, J., Sun, S., Li, X., Jensen, M.A., Hartono, N.T.P., Nienhaus, L., Wieghold, S., et al. (2019). Homogenized halides and alkali

cation segregation in alloyed organic-inorganic perovskites. Science *363*, 627–631.

31. Hall, A.S., Lavery, L.L., and Doux, P. (2018). Effective multimodal multiscale analytical and imaging correlation. IEEE Sens. Lett. *3*, 1–4.

32. Hawash, Z., Ono, L.K., and Qi, Y. (2016). Moisture and oxygen enhance conductivity of LiTFSI-doped Spiro-MeOTAD hole transport layer in perovskite solar cells. Adv. Mater. Interfaces *3*, 1600117.

33. Wang, S., Sina, M., Parikh, P., Uekert, T., Shahbazian, B., Devaraj, A., and Meng, Y.S. (2016). Role of 4-tert-butylpyridine as a hole transport layer morphological controller in perovskite solar cells. Nano Lett. *16*, 5594–5600.

34. Law, C., Miseikis, L., Dimitrov, S., Shakya-Tuladhar, P., Li, X., Barnes, P.R.F., Durrant, J., and O'Regan, B.C. (2014). Performance and stability of lead perovskite/TiO$_2$, polymer/PCBM, and dye sensitized solar cells at light intensities up to 70 suns. Adv. Mater. *26*, 6268–6273.

35. Bing, J., Kim, J., Zhang, M., Zheng, J., Lee, D.S., Cho, Y., Deng, X., Lau, C.F.J., Li, Y., Green, M.A., et al. (2019). The impact of a dynamic two-step solution process on film formation of Cs$_{0.15}$(MA$_{0.7}$FA$_{0.3}$)$_{0.85}$PbI$_3$ perovskite and solar cell performance. Small *15*, e1804858.

36. Bing, J., Lee, D.S., Zheng, J., Zhang, M., Li, Y., Kim, J., Lau, C.F.J., Cho, Y., Green, M.A., Huang, S., et al. (2019). Deconstruction-assisted perovskite formation for sequential solution processing of Cs$_{0.15}$(MA$_{0.7}$FA$_{0.3}$)$_{0.85}$PbI$_3$ solar cells. Sol. Energy Mater. Sol. Cells *203*, 110200.

37. Jung, K., Lee, J.H., Oh, K., Im, C., Do, J., Kim, J., Chae, W.S., and Lee, M.J. (2018). Efficient composition tuning via cation exchange and improved reproducibility of photovoltaic performance in FA$_x$MA$_{1-x}$PbI$_3$ planar heterojunction solar cells fabricated by a two-step dynamic spin-coating process. Nano Energy *54*, 251–263.

38. Wang, S., Yuan, W., and Meng, Y.S. (2015). Spectrum-dependent Spiro-OMeTAD oxidization mechanism in perovskite solar cells. ACS Appl. Mater. Interfaces *7*, 24791–24798.

39. Wang, S., Huang, Z., Wang, X., Li, Y., Günther, M., Valenzuela, S., Parikh, P., Cabreros, A., Xiong, W., and Meng, Y.S. (2018). Unveiling the role of tBP-LiTFSI complexes in perovskite solar cells. J. Am. Chem. Soc. *140*, 16720–16730.

40. Li, W., Dong, H., Wang, L., Li, N., Guo, X., Li, J., and Qiu, Y. (2014). Montmorillonite as bifunctional buffer layer material for hybrid perovskite solar cells with protection from corrosion and retarding recombination. J. Mater. Chem. A *2*, 13587–13592.

41. Saliba, M., Correa-Baena, J.P., Wolff, C.M., Stolterfoht, M., Phung, N., Albrecht, S., Neher, D., and Abate, A. (2018). How to make over 20% efficient perovskite solar cells in regular (*n-i-p*) and inverted (*p-i-n*) architectures. Chem. Mater. *30*, 4193–4201.

42. Liu, Z., Hu, J., Jiao, H., Li, L., Zheng, G., Chen, Y., Huang, Y., Zhang, Q., Shen, C., Chen, Q., and Zhou, H. (2017). Chemical reduction of intrinsic defects in thicker heterojunction planar perovskite solar cells. Adv. Mater. *29*, 1606774.

43. Zhou, Y., Vasiliev, A.L., Wu, W., Yang, M., Pang, S., Zhu, K., and Padture, N.P. (2015). Crystal morphologies of organolead trihalide in mesoscopic/planar perovskite solar cells. J. Phys. Chem. Lett. *6*, 2292–2297.

44. Rothmann, M.U., Li, W., Zhu, Y., Liu, A., Ku, Z., Bach, U., Etheridge, J., and Cheng, Y.B. (2018). Structural and chemical changes to CH$_3$NH$_3$PbI$_3$ induced by electron and gallium ion beams. Adv. Mater. *30*, e1800629.

45. Yang, Y., Davies, D.M., Yin, Y., Borodin, O., Lee, J.Z., Fang, C., Olguin, M., Zhang, Y., Sablina, E.S., Wang, X., et al. (2019). High-efficiency lithium-metal anode enabled by liquefied gas electrolytes. Joule *3*, 1986–2000.

46. Lee, J.Z., Wynn, T.A., Schroeder, M.A., Alvarado, J., Wang, X., Xu, K., and Meng, Y.S. (2019). Cryogenic focused ion beam characterization of lithium metal anodes. ACS Energy Lett. *4*, 489–493.

47. Hawash, Z., Ono, L.K., Raga, S.R., Lee, M.V., and Qi, Y. (2015). Air-exposure induced dopant redistribution and energy level shifts in spin-coated Spiro-Meotad films. Chem. Mater. *27*, 562–569.

48. Jung, M.C., Raga, S.R., Ono, L.K., and Qi, Y. (2015). Substantial improvement of perovskite solar cells stability by pinhole-free hole transport layer with doping engineering. Sci. Rep. *5*, 9863.

49. Kato, Y., Ono, L.K., Lee, M.V., Wang, S., Raga, S.R., and Qi, Y. (2015). Silver iodide formation in methyl ammonium lead iodide perovskite solar cells with silver top electrodes. Adv. Mater. Interfaces *2*, 1500195.

50. Yuan, W., Zhao, H., Hu, H., Wang, S., and Baker, G.L. (2013). Synthesis and characterization of the hole-conducting silica/polymer nanocomposites and application in solid-state dye-sensitized solar cell. ACS Appl. Mater. Interfaces *5*, 4155–4161.

51. Vinodh, M.S., and Jeurgens, L.P.H. (2004). Quantitative analysis of angle-resolved XPS spectra recorded in parallel data acquisition mode. Surf. Interface Anal. *36*, 1629–1636.

52. Xie, H., Liu, X., Lyu, L., Niu, D., Wang, Q., Huang, J., and Gao, Y. (2016). Effects of precursor ratios and annealing on electronic structure and surface composition of CH$_3$NH$_3$PbI$_3$ perovskite films. J. Phys. Chem. C *120*, 215–220.